Norihisa Usui · Hiroyuki Tsujino · Yosuke Fujii ·
Masafumi Kamachi

Short-range prediction experiments of the Kuroshio path variabilities south of Japan

Abstract Assimilation and prediction experiments of the Kuroshio path variability south of Japan were conducted to investigate the predictability of the Kuroshio path. The assimilation and prediction system is composed of an eddy-resolving model and a three-dimensional variational analysis scheme with vertical coupled temperature–salinity empirical orthogonal function modes. The sea surface height (SSH) variability and the variations of the Kuroshio path of the assimilation fields are in good agreement with those observed. The results of the assimilation are then used as the initial conditions for 138 cases of 90-day prediction experiments conducted from 1993 to 2004. The predictive limit of our system is assessed by the SSH anomaly in the assimilation field and is found to be around 40–60 days, which is much longer than that of the persistence. The prediction results show good performance in the transition stage from a straight to a meandering path. For example, a large meandering event that occurred in August 2004 is successfully predicted in a 2-month forecast. Two types of failure cases are investigated. One is a case where the eastward propagation speed of the meander is faster than a real state. The dynamical response of the model to the assimilation revealed that an initial shock, caused by the dynamically unbalanced initial condition, induces the fast eastward propagation of the meander. The other case exhibits an unrealistic meander. In this case, a cold anomaly at an intermediate layer in the initial condition grows rapidly and results in the unrealistic meander. This implies that the Kuroshio path south of Japan has a chaotic nature. These facts revealed by the failure cases give us some insight for improving the predictive skill of the Kuroshio path variability.

Keywords Kuroshio path · Kuroshio large meander · Data assimilation · Short-range prediction · Predictive limit · Baroclinic instability

1 Introduction

The Kuroshio, the western boundary current of the North Pacific subtropical gyre, flows northeastward along the continental slope of the East China Sea, turns east through the Tokara Strait, and proceeds eastward along the southern coast of Japan until it separates from the coast and enters the Pacific basin as a free jet called the Kuroshio Extension. It has a significant impact on the climate around Japan because of its large heat transport. Also, the variations of the Kuroshio path have a large influence on fisheries, ship navigation, marine resources, etc. Therefore, it has been studied by many researchers.

Yoshida (1964) and Taft (1972) showed that the Kuroshio path south of Japan exhibits remarkable bimodal features, namely, the large meander path and the nonlarge meander path. Kawabe (1985) classified three typical paths (Fig. 1): the typical large meander path (tLM), the offshore nonlarge meander path (oNLM), and the nearshore nonlarge meander path. The duration of the large meander and the nonlarge meander paths is from a few years to a decade. The large meander occurs with the most predominant period of about 20 years (Kawabe 1987). The variations of the Kuroshio path and their relation to velocity, volume transport, and upstream position of the Kuroshio were investigated from the long time series of hydrographic data and tide gauge records (Kawabe 1995). After the launch of the ocean topography experiment (TOPEX)/Poseidon in 1992, altimeter-derived sea surface height (SSH) became widely available and enabled us to capture oceanic variations, including the variations of the Kuroshio path. Imawaki et al. (1996) successfully detected

N. Usui (✉) · H. Tsujino · Y. Fujii · M. Kamachi
Oceanographic Research Department,
Meteorological Research Institute,
Nagamine 1-1,
Tsukuba, 305-0052, Japan
e-mail: nusui@mri-jma.go.jp

Fig. 1 Typical stable paths of the Kuroshio south of Japan (Kawabe 1995). Abbreviations are *nNLM* the nearshore non-large meander path, *oNLM* the offshore nonlarge meander path, and *tLM* the typical large meander path
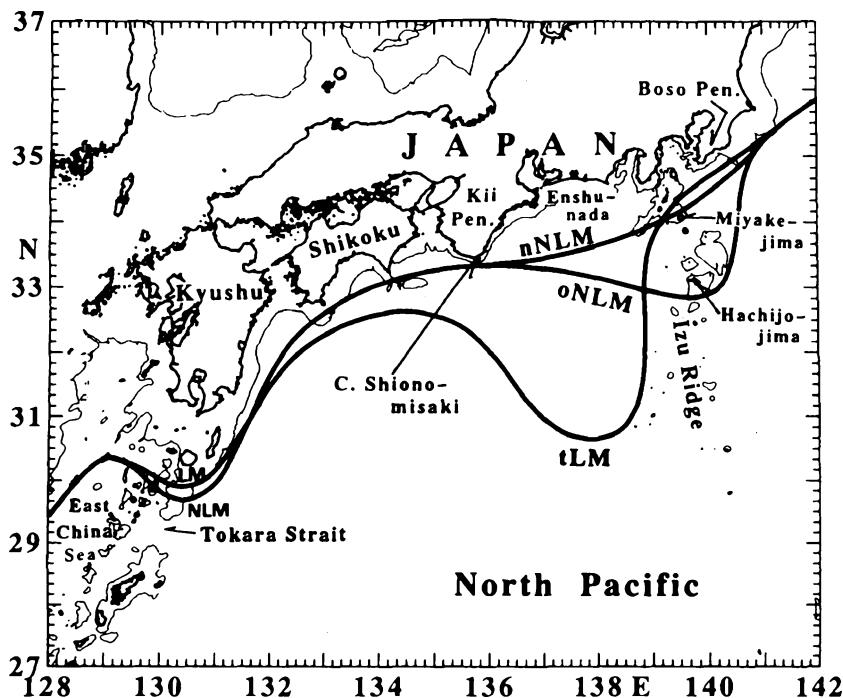
the fluctuations of the Kuroshio axis south of Japan using the TOPEX/Poseidon altimeter data. Ebuchi and Hanawa (2001) investigated the trajectory of the mesoscale eddies in the Kuroshio recirculation region and pointed out that the interaction between the mesoscale eddy and the Kuroshio east of the Kyushu may trigger meanders. Many other studies using satellite altimeter data have discussed the relationship between the formation of the meander of the Kuroshio and the mesoscale eddies (e.g., Mitsudera et al. 2001; Ebuchi and Hanawa 2003; Waseda et al. 2003). Many theoretical and numerical studies have also addressed mechanisms of the Kuroshio path variations (e.g., Robinson and Taft 1972; Masuda 1982; Yoon and Yasuda 1987). During the 1990s, many modeling studies with somewhat idealized settings have reported descriptions of the Kuroshio path variations (e.g., Sekine 1990; Endoh and Hibiya 2000, 2001; Akitomo et al. 1997; Hurlburt et al. 1996; Qiu and Miao 2000). Recently, an eddy-resolving model simulation with realistic settings (e.g., Miyazawa et al. 2004; Tsujino et al. 2006) has become feasible in step with the development of computing power.

In addition to the background described above, the development of ocean data assimilation in the past decade enables us to nowcast and forecast the ocean states. Many groups have attempted to construct an assimilation and prediction system and examined the predictability in some regions. Mellor and Ezer (1991) conducted assimilation and prediction experiments for the Gulf Stream region using a primitive equation model and a nudging assimilation technique. They obtained a predictive limit of 20 days. Brasseur et al. (1996) used a quasigeostrophic model of the Atlantic basin with a technique of nudging the TOPEX/Poseidon altimeter data. They also obtained a predictive

limit of about 20 days. The predictability of the variations of the Kuroshio path has also been examined by some groups. Hurlburt et al. (2000) and Rhodes et al. (2002) developed an operational nowcast/forecast system for the North Pacific and performed 1-month forecast experiments in the Kuroshio region. The system consists of a layered primitive equation model and an assimilation scheme based on optimum interpolation. They concluded that their prediction skill is longer than 30 days, which is better than the persistence and the climatology. Komori et al. (2003) conducted prediction experiments of the Kuroshio path variabilities using a 1–1/2-layer shallow water model and a two-dimensional variational scheme with a weak constraint. They concluded that the predictive limit is about 60 days. Kamachi et al. (2004) also conducted assimilation and prediction experiments using an operational data assimilation and prediction system. Their assimilation results reproduced the formation process of the meander quite well. They concluded that the predictive limit is from 20 to 80 days, which depends on the transition stages of the meander. Most of these studies on the prediction of the Kuroshio path have focused on the statistical properties of the prediction results to assess the predictive limit. Komori et al. (2003) investigated examples of success and failure by looking at the vorticity balance. They concluded that the cause of the failure was the lack of certain dynamical processes in the shallow water model, such as the effects of baroclinic instability and bottom topography.

In this study, we will try to predict the Kuroshio path variability south of Japan using an ocean data assimilation and prediction system with realistic settings to assess the predictive limit of our system and reveal any defects of our system. By doing so, we can explore the strategy for improving the predictability of the Kuroshio path. Usui et

al. (2006) have already verified the assimilation system (e.g., temperature and salinity profiles, current transport around Japan), which showed a good agreement with the independent observations. We therefore focus on the predictability of the Kuroshio path for the first step of the assessment of the prediction system. This study also follows Tsujino et al. (2006), who investigated the transition process between the bimodal paths of the Kuroshio using a free simulation based on the same model as ours. The verification of their results is also one of the objectives of this study. This paper is organized as follows: descriptions of the prediction system and experimental conditions are described in Section 2. General features of the experimental results and case studies are described in Sections 3 and 4, respectively. Results are summarized in Section 5.

2 Description of prediction system and experiments

2.1 Dynamical model

We use the Meteorological Research Institute Community Ocean Model (MRI.COM; Ishikawa et al. 2005) for the dynamical model. MRI.COM is a multilevel model that solves primitive equations under the hydrostatic and the Boussinesq approximation. A free-surface option of Killworth et al. (1991) is selected to solve the barotropic part of the equations. The vertical coordinate near the surface follows the surface topography-like σ -coordinates, which enables us to adopt a fine vertical resolution near the surface. For the nonlinear momentum advection, the generalized enstrophy-preserving scheme (Arakawa 1966) and the scheme that contains the concept of diagonally upward/downward mass momentum fluxes along the sloping bottom are applied. Performance of a fine-resolution model with this scheme is described by Ishizaki and Motoi (1999). For tracer advection, a modified version of the Quadratic Upstream Interpolation for Convective Kinematics scheme (Holland et al. 1998) is applied. A biharmonic operator is used for horizontal turbulent mixing with 1.0×10^{10} m^4 s^{-1} as diffusivity coefficient. A biharmonic friction with a Smagorinsky-like viscosity (Griffies and Hallberg 2000) is used for momentum. The vertical viscosity and diffusivity are determined by the turbulent closure scheme of Noh and Kim (1999). The bottom friction is calculated according to the formula proposed by Weatherly (1972). A sea ice model with the thermodynamics of Mellor and Kantha (1989) and the elastic–viscous–plastic rheology of Hunke and Ducowicz (2002) is also applied.

The model domain spans from 117°E to 160°W zonally and from 15°N to 65°N meridionally (Fig. 2). The horizontal resolution is variable: it is 1/10° from 117°E to 160°E and 1/6° from 160°E to 160°W zonally, and it is 1/10° from 15°N to 50°N and 1/6° from 50°N to 65°N meridionally. There are 54 layers in the vertical with thickness increasing from 1 m at the surface to 250 m near the bottom. Oceanic states at the side boundaries are replaced by those from the low-resolution model (one-way

nesting). The nesting method is based on that of Spall and Holland (1991). The model domain of the low-resolution model spans from 100°E to 75°W zonally and from 15°S to 65°N meridionally. The domain is closed, i.e., the Indonesian Passage and the Bering Strait are closed. At the southern end of the model domain (from 15°S to 13°S) of the low-resolution model, temperature and salinity are restored to the climatology (Ocean Climate Laboratory 1999) from top to bottom with a restoring time of 120 days. The horizontal resolution is 1/2°. The vertical grid spacing is the same as that of the 1/10° model. The bottom topographies for both models are based on Smith and Sandwell's (1997). More detailed descriptions of the model are given by Tsujino et al. (2006).

2.2 Assimilation scheme

We use the Meteorological Research Institute Multivariate Ocean Variational Estimation (MOVE) system (Usui et al. 2006) for the assimilation system. The analysis scheme adopted in the MOVE system is a multivariate three-dimensional variational (3DVAR) analysis scheme with vertical coupled temperature–salinity (T–S) empirical orthogonal function (EOF) modal decomposition (Fujii and Kamachi 2003a). Amplitudes of the T–S EOF modes above 1,500 m are employed as control variables. Dominant modes can be understood as the first and second baroclinic modes, changes of the water properties near the surface, change of water mass properties, and so on (see Fujii and Kamachi 2003b). T–S EOF modes are different in regions with different hydrographic features (e.g., subtropical/subpolar regions and marginal seas). In this system, the model region is divided into 10 subregions (Fig. 2), which are decided empirically, and vertical T–S EOF modes are calculated from the observed T–S profiles for each subregion. We employ the first 12 modes for the 3DVAR, which explain more than 85% of the total variance.

The cost function $J(y)$ is defined as follows:

$$
\begin{aligned}
J(y) = & \frac{1}{2} \sum_l \sum_m y_{l,m}^T B_{l,m}^{-1} y_{l,m} \\
& + \frac{1}{2} \sum_i \left[H_i x(y) - x_i^O \right]^T R_i^{-1} \left[H_i x(y) - x_i^O \right] \\
& + \frac{1}{2\sigma_h^2} \sum_j \left[\mathcal{H}_j(x(y)) - h_j^O \right]^2 \\
& + \frac{1}{2\alpha} \sum_p \sum_k \left[\mathcal{D}\{\rho_{p,k}(x) - \rho_{p,k+1}(x)\} \right]^2,
\end{aligned}
\tag{1}
$$

where y is the amplitude of the vertical coupled T–S EOF modes. Subscripts l and m denote the l-th mode and m-th subregion, respectively. Matrices B and R are the background and observation error covariance matrices, respectively. It should be noted that B is a nondiagonal matrix because it includes the horizontal correlations among

Fig. 2 a Model domain and **b** subregions for the T–S EOF modes. Bathymetry is marked with contour intervals of 1,000 m. The model domain is divided into 10 subregions. A set of T–S EOF modes is calculated in each subregion

(a) model domain and bottom topography

(b) subregions for T–S EOF mode
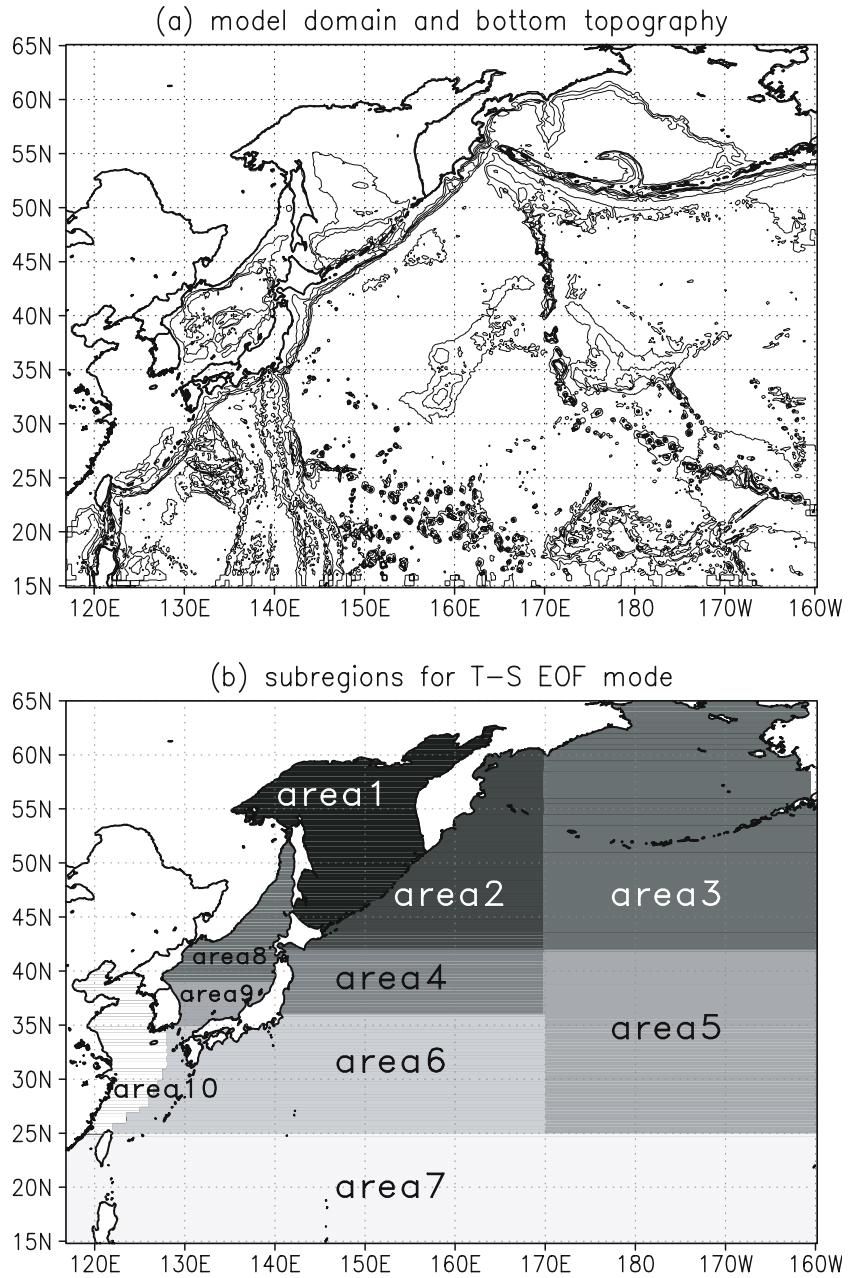
background errors (see Fujii and Kamachi 2003b). The Gaussian function is adopted as the horizontal correlation model in the background covariance matrix B. The e-folding scales in the horizontal correlation model are decided from Kuragano and Kamachi (2000). The background (observation) error variance σ_b^2 (σ_o^2) and the diagonal elements of B (R) are decided by a parameter μ as follows (Fujii and Kamachi 2003c):

$$\sigma_b^2 = (1-\mu)\sigma^2, \ \ \sigma_o^2 = \mu\sigma^2, \tag{2}$$

where the scalar value σ, which varies horizontally and vertically, is the reference value estimated from the observed data. The observation error σ_o^2 includes the measurement and representativeness errors. The scalar value μ is set to 0.4. The vector x_i^O is the i-th observation profile of temperature and salinity, and h_j^O is the j-th sea surface dynamic height (SDH) data, the sum of the mean SDH and SSH anomaly (SSHA) measured by satellite altimetry. The mean SDH is calculated from observed mean temperature and salinity fields from 1993 to 1999. The coefficient σ_h is the observation error of SSHA, which is set to the constant value of 10 cm. Considering the representativeness error of the operator $\mathcal{H}$ described later, σ_h is set to a somewhat large value compared with a measurement error of the satellite altimeter. The matrix H is the observation operator for the temperature and salinity profiles, by which the temperature and salinity in the model

space are linearly interpolated into those in the observation space. The nonlinear operator $\mathcal{H}$ estimates a SDH from temperature and salinity in the model field as follows:

$$\mathcal{H}(x) = -\frac{1}{\rho_s} \int_0^{z_m} \rho'(x, p)dz, \tag{3}$$

where ρ_s is the surface density, z_m is the reference depth, ρ' is the difference of density from the reference state, and p is pressure. We use 0°C and 35.0 psu as the reference state, and 1,500 m as the reference depth. We checked the validity of the operator $\mathcal{H}$ using the result of a free model simulation. In the south of Japan, the target area of the prediction experiment, more than 80% of the SSH variances is explained by the SDH from the operator $\mathcal{H}$, although it does not include the barotropic contributions (not shown).

The first term on the right-hand side of Eq. (1) denotes the deviation from the first-guess. The second and third terms on the right-hand side of Eq. (1) denote deviations from the observed T–S profile and the SSH derived from satellite altimetry, respectively. The fourth term on the right-hand side of Eq. (1) denotes the constraint for avoiding density inversion (Fujii et al. 2005). The scalar value $\rho_{p,k}$ is the density at the p-th grid point and k-th layer ($k = 0$: surface). The function $D(x)$ is written as follows: $D(x) = 0$ when $x < 0$, and $D(x) = x$ when $x > 0$. Thus, the minimization scheme acts to eliminate density inversion, that is, when $x > 0$. The preconditioned optimizing utility for large-dimension analysis (Fujii and Kamachi 2003c; Fujii 2005) is applied for minimizing the nonlinear cost function. The scheme can minimize the nonlinear cost function without inversion of the background error covariance matrix.

The vector x, the state vector of temperature and salinity profiles, is transformed from the control variable y as follows:

$$x(y) = x_f + S \sum_l w_l U_l \Lambda_l y_l, \tag{4}$$

where x_f is the first-guess, S is the matrix composed of dominant T–S EOF modes, Λ is the diagonal matrix whose elements are the singular value of T–S EOF modes, and w_l is the weight coefficient for the l-th subregion, which has to satisfy $\sum_l w_l^2 = 1$ (Fukumori 2002). In the buffer zone located around the boundary between subregions (not shown in Fig. 2), w_l^2 varies linearly from 0 to 1 along latitude or longitude.

The 3DVAR results are inserted into the model temperature and salinity fields above 1,500 m by the incremental analysis updates (IAU; Bloom et al. 1996). In this system, the IAU is implemented as follows: (1) The model is integrated until the middle of the assimilation period without any correction. The model output at this time is used as a first-guess for all observations within the assimilation period. (2) The 3DVAR is implemented and analysis increments are transformed into a constant forcing

by dividing by the number of time steps corresponding to the assimilation period. (3) The model is restarted from half of an assimilation period prior to the analysis time, and integrated during the assimilation period with the constant forcing. (4) At the end of the assimilation period, the model results are output and used as initial conditions for the prediction experiments. Steps (1–4) are repeated.

2.3 Experimental conditions

The assimilation experiment was conducted from January 1993 to September 2004. The assimilation period is 1/3 month: the first and second assimilation periods in a month are 10 days and the third one varies from 8 to 11 days. Temperature and salinity profiles above 1,500 m and SSHA data are assimilated. Temperature and salinity data are collected from World Ocean Database 2001 and the Global Temperature–Salinity Profile Program database (Hamilton 1994). The SSHA data is the along-track data from the TOPEX/Poseidon, Jason-1, European remote sensing satellite (ERS)-1/2, and environmental satellite altimeters, which are extracted from the segment sol multimission altimetry and orbitography/data unification and altimeter combination system delayed-time multimission altimeter products (CLS 2004). The model is driven by wind-stress and heat fluxes from the National Centers for Environmental Prediction (NCEP)—Department of Energy Atmospheric Intercomparisons project reanalysis (Kanamitsu et al. 2002; hereafter NCEP2). Latent and sensible heat fluxes are recalculated in the model using model sea surface temperature and the bulk formula of Kondo (1975). The fresh water flux is corrected by restoring sea surface salinity toward the monthly mean climatology with a restoring time of 1 day to prevent a model drift.

One hundred thirty eight cases of prediction experiments for the Kuroshio path variability south of Japan were conducted from February 1993 to July 2004. Predictions start on the first day of every month and are integrated for 90 days. The wind-stress and heat fluxes used in the prediction experiments are NCEP2, the same as in the assimilation experiment. We should treat an external forcing as an unknown factor in the prediction. However, we treat it here as a known factor because our objective is to assess the predictive skill of the assimilation scheme and the dynamical model when a perfect external forcing is given. The predictive skill obtained from this protocol could be affected by the use of predictive forcing.

3 General features of experimental results

3.1 Assimilation fields

The assimilation results (e.g., temperature and salinity profiles, current transport around Japan) have already been verified by Usui et al. (2006), who showed that the assimilation result reproduced the observed features well.

In this subsection, we therefore discuss the reproducibility of the SSH and the Kuroshio path variations in the assimilation fields, which will impact on the Kuroshio path prediction.

Figure 3 shows the mean and the standard deviation of SSH for the assimilation and the observations. The averaging period is from 1993 to 2001, when TOPEX/Poseidon and ERS-1/2 data are available. The observation data are a multisatellite-gridded SSH-derived product from TOPEX/Poseidon and ERS-1/2 (Kuragano and Kamachi 2003), with $1/2°$ resolution. The spatial distribution of the SSH variability in the assimilation field shows good agreement with the altimeter observations. It should be noted that the amplitude of the SSH variability of the assimilation field is somewhat larger than that of the observations because of the difference in spatial resolution. In fact, the SSHA power spectra of the assimilation field and the observed field along a TOPEX/Poseidon ground track show good agreement (not shown here). The mean SSH field also reflects the observed features. Note that the observed mean SSH is obtained from the climatological hydrographic data using Eq. (1). The observed SSH field

therefore is somewhat smoothed compared with the assimilation field.

Figure 4 compares the location of the Kuroshio axis along 138° E determined from the assimilation and the observations, which is a good indicator of the Kuroshio path type. The period is also from 1993 to 2001. The observed Kuroshio axis is estimated every 10 days from satellite altimetry (TOPEX/Poseidon and ERS-1/2) and surface drifting buoys (Ambe et al. 2004). The position of the Kuroshio axis in the assimilation field is defined as the latitude of the maximum surface velocity, as in Ambe et al. (2004). The Kuroshio axis in the assimilation field closely follows the observed one during the whole period.

3.2 Predicted fields

Figure 5 compares the location of the Kuroshio axis along 138° E determined from the prediction and the assimilation. The Kuroshio follows a nonlarge meander path from 1993 to the middle of 2004, after which the Kuroshio undergoes a large meander path. The following features can be seen in the prediction results. The Kuroshio axes in the prediction field follow those in the assimilation field comparatively well in the transition stages from a straight to a meander path. In contrast, the predicted Kuroshio axes tend to shift from a meander to a straight path earlier. These two features are reported in previous studies, too (e.g., Komori et al. 2003; Kamachi et al. 2004). Also, unrealistic meanders can be seen in some results. These features seen in the prediction results will be discussed in the next section.

Next, we show some statistical properties of the prediction results to assess the predictive limit of our system. The prediction results are assessed by the assimilation results, because the assimilation results reproduce the real state quite well, as described above. Figure 6 shows the spatial distribution of the normalized root mean square (RMS) difference of SSHA between the prediction and the assimilation at each forecast time. SSHA is suitable for assessing a prediction result because it reflects the internal state of the ocean. The RMS difference is estimated from the mean SSH over each assimilation period (1/3 month). The standard deviation of SSH estimated in each 1/3 month is used to normalize the RMS difference. The forecast time is taken as 10-day intervals in all cases, although it actually varies from 8 to 11 days. The spatial distribution of the normalized RMS difference shows that the prediction results have a relatively large error southeast of Kyushu and off Enshu-nada. The error at the southeast of Kyushu, which is related to unrealistic meanders occurring south of Shikoku as described later, seems to propagate along the Kuroshio from the Tokara Strait to south of Shikoku. The error off Enshu-nada probably results from a weak cold-eddy formed on the shoreward side of the Kuroshio (not shown). However, we note that the absolute value of the RMS difference off Enshu-nada is not so large because the standard deviation of SSH off Enshu-nada is small (Fig. 3b).
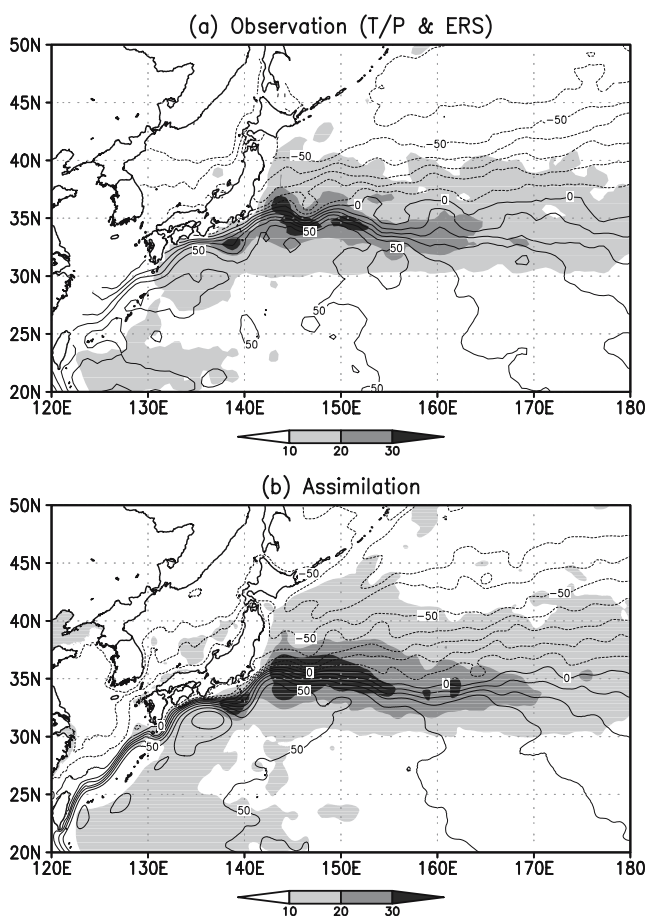

Fig. 3 Standard deviation (*shades*) and mean (*contours*) of SSH from 1993 to 2004 for **a** observation (TOPEX/Poseidon and ERS) and **b** assimilation fields

Fig. 4 Time series of the latitude of the Kuroshio axis along 138°E from **a** the observation (*thin line*; Ambe et al. 2004) and **b** the assimilation (*thick line*) fields
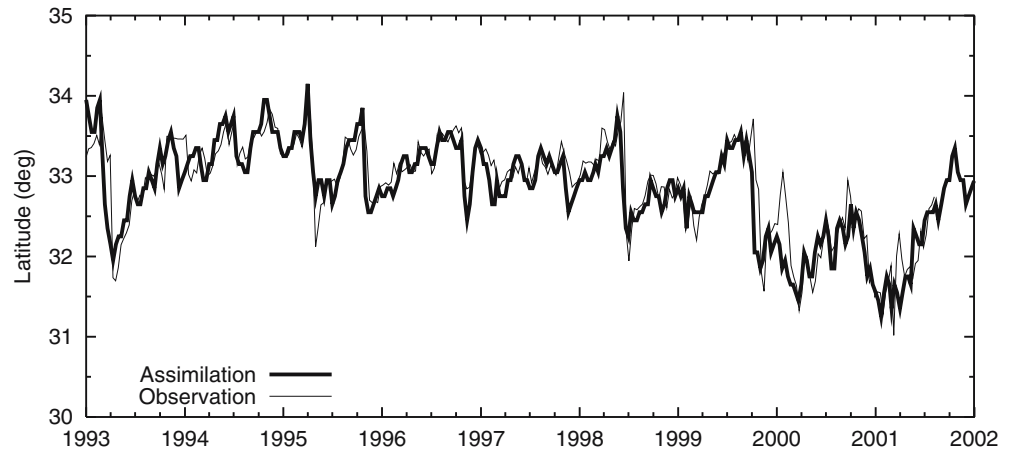
Figure 7 shows the spatial distribution of SSH bias, which is the mean SSH difference between the prediction and the assimilation fields. The SSH bias south of Japan shows a remarkable contrast between positive values west of the Izu Ridge and negative ones south of the Kii Peninsula. This difference is due to a eastward movement of a warm eddy south of the Kii Peninsula in the prediction. The warm eddy in the model free run (without assimilation) is located further south than in the assimilation (not shown), probably due to the broader Kuroshio axis in the model free run. The eddy tends to be advected eastward by the Kuroshio in the prediction, because it is initialized in a realistic position which is closer to the Kuroshio axis than the model free run. In addition, the eastward movement of

the warm eddy might contribute to the transition of the Kuroshio axis from a meander to a straight path, as described by Ebuchi and Hanawa (2003). It implies that the reduction of the model bias is crucial for the accurate prediction of the Kuroshio path. However, the SSH bias is comparatively small compared with the standard deviation of SSH (Fig. 3). In fact, the RMS difference calculated from the SSH after bias removal is almost the same as that without the bias removal. It implies that most of the errors in the prediction are random. These errors and their causes will be described in more detail with case studies in the next section.

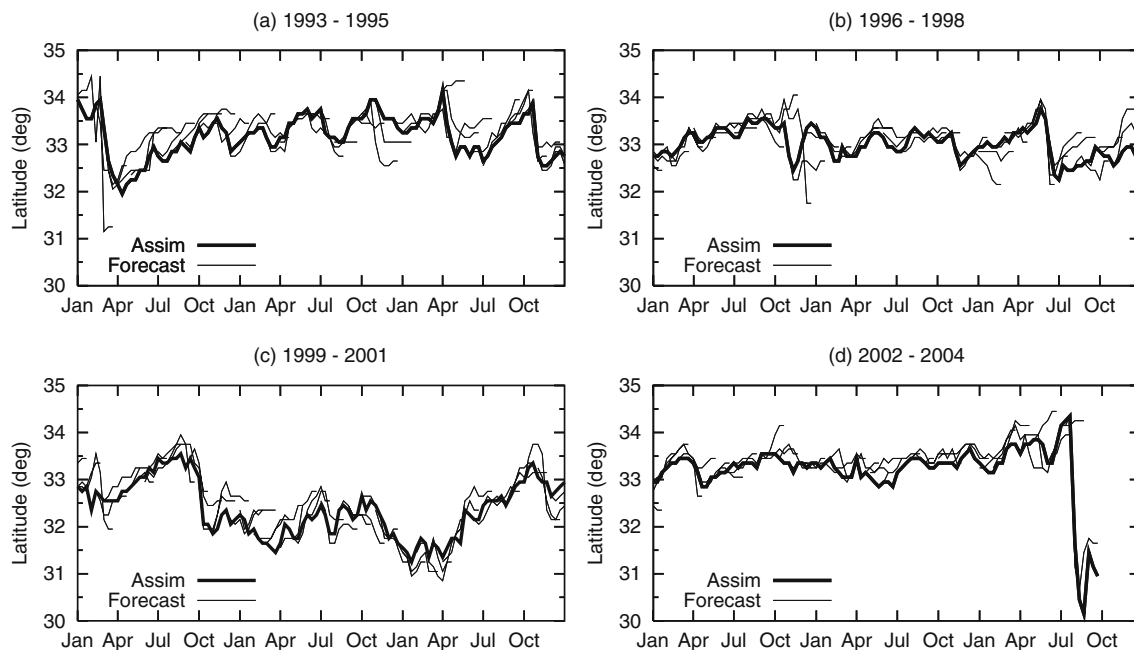Figure 8 shows a time evolution of the SSH RMS difference in the rectangular region (131°–140° E, 30° –

Fig. 5 As in Fig. 4 but for the forecast (*thin line*) and the assimilation (*thick line*) fields for **a** 1993–1995, **b** 1996–1998, **c** 1999–2001, and **d** 2002–2004
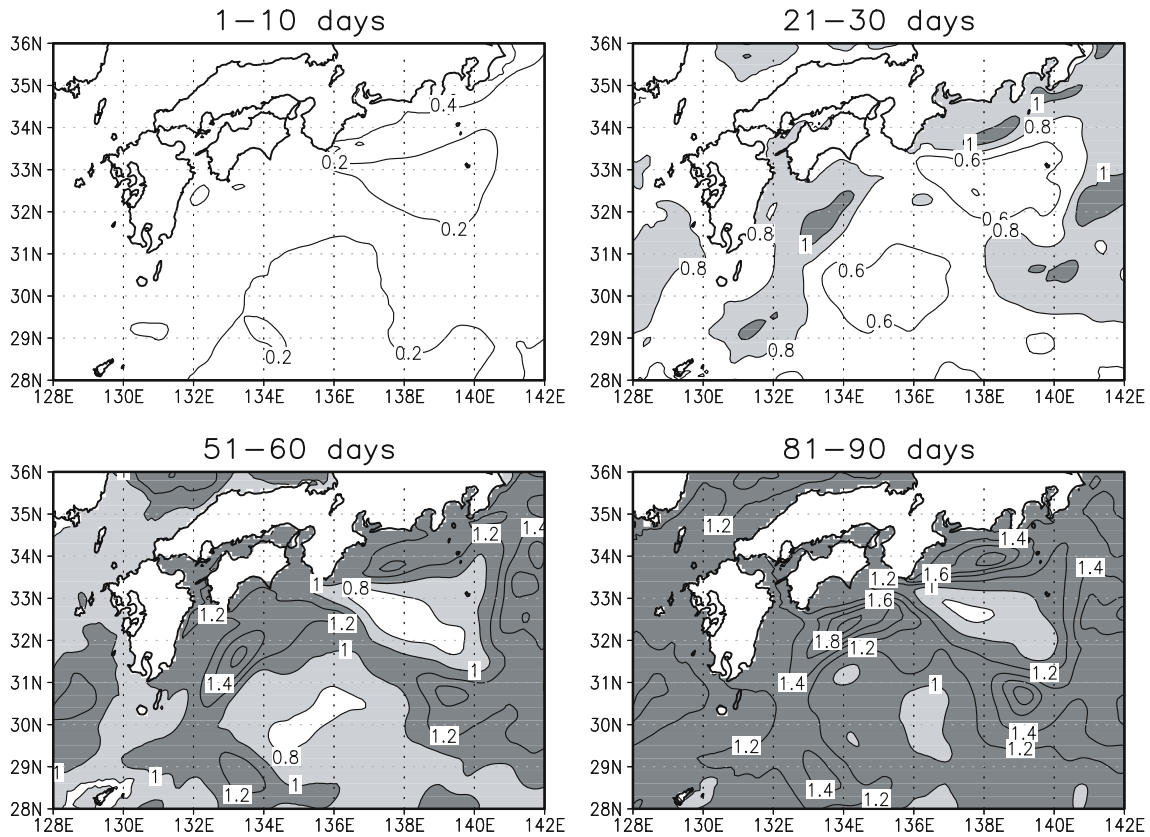
Fig. 6 Time evolution of the normalized RMS difference in SSH between the prediction and assimilation fields at each forecast time. *Units* are nondimensional. *Light* and *dark shading* corresponds to the area where the normalized RMS differences are greater than 0.8 and 1.0, respectively

35° N), the average value of 138 cases. The error bar denotes the standard deviation calculated from the 138 cases. The result of a persistence, which assumes that SSHA does not change from an initial condition, is also shown. We note that seasonal changes in the SSH field are expressed in the persistence because SSHA is defined here as the anomaly from the 1/3-monthly mean SSH. Eliminating the seasonal variation in the assimilation field, and using standard deviation of SSH of 13.5 cm depicted in Fig. 8 as a threshold for a predictive limit, we find that the predictive limit of our system is roughly 40–60 days, which is much longer than that of the persistence.

4 Case studies

As described in the previous section, the prediction performance depends on the transition stages of a meander. The prediction shows a relatively good performance in the transition stage from a straight to a meander path, while the prediction performance deteriorates in the transition stage from a meander to a straight path. Also, some predictions show unrealistic meanders. In this section, these three features seen in the prediction results are investigated in more detail with case studies.

4.1 Case 1 (transition from a straight to a meander path)

We present here a prediction result initialized on 1 July 2004 as an example of success. Figure 9 shows the temperature and velocity at 200 m in the assimilation and prediction fields. The small meander, located in the south of the Kii Peninsula at the beginning of July 2004, grows as it propagates eastward and develops into a large meander path, the tLM, in the middle of August 2004. After that, the Kuroshio sustains the large meander path. These processes are successfully predicted.

Tsujino et al. (2006) investigated an evolution process of a large meander in a free model simulation, and pointed out that an interaction between the upper-layer eddies and a deep anticyclonic eddy plays a significant role in the evolution of a large meander. The evolution process of the large meander in this case is shown in Fig. 10 with SSH and velocity at 3,000 m. A deep anticyclonic eddy can be seen in this case too. It is located between upper-layer cold and warm eddies. The meander develops into a large meander under this phase relation. At the final stage of the evolution, the deep anticyclonic eddy becomes in-phase with the upper-layer warm eddy. Thus, the evolution process of the large meander in this case is also understood as a growth of the baroclinic instability as in Tsujino et al. (2006). The
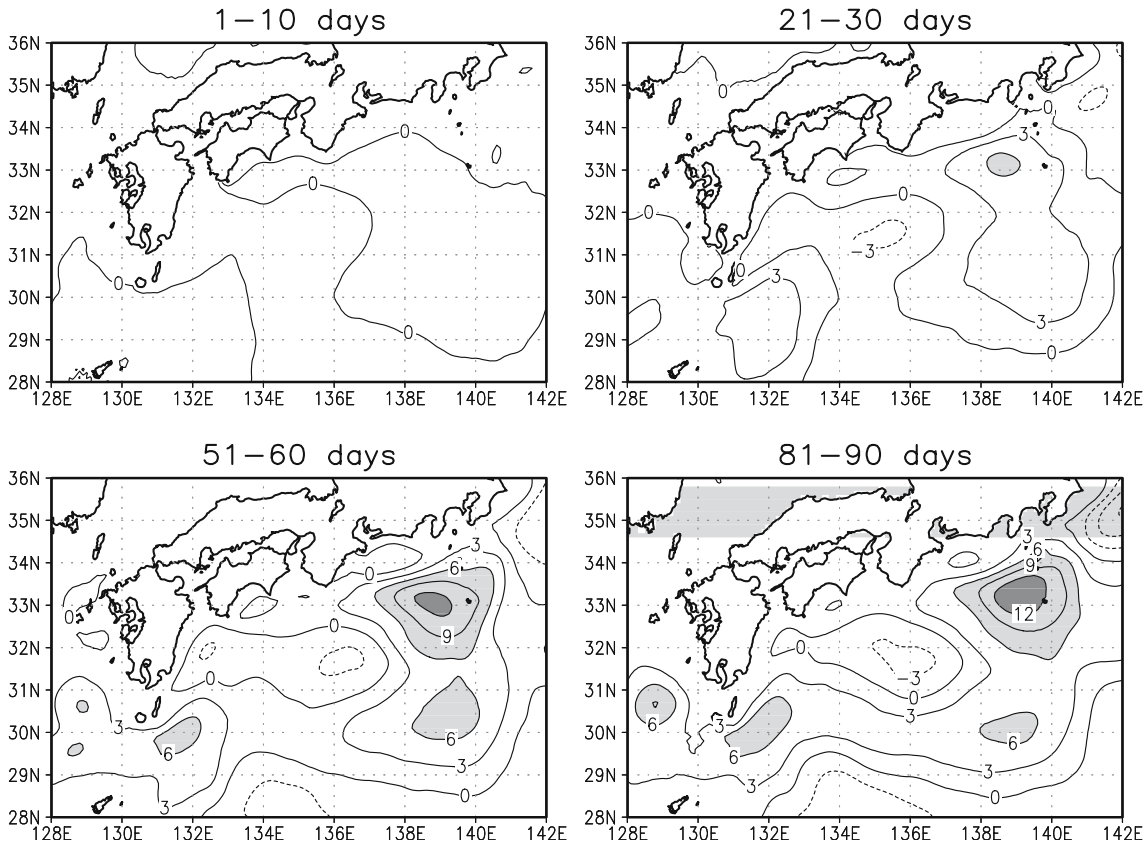
Fig. 7 Time evolution of the SSH bias (unit in cm) for each forecast time. *Light* and *dark shading* corresponds to the area where the SSH biases are greater than 6 cm and 12 cm, respectively

Fig. 8 Time evolution of the RMS difference in SSH between the prediction and the assimilation fields. *Thick solid line with squares* and the *dashed line* denote the dynamical prediction and the persistence, respectively. *Error bars* denote the standard deviation of SSH RMS differences in all cases. The *dotted line* of 13.5 cm is the standard deviation of SSH in the assimilation field

evolution process of the oNLM can also be explained by a baroclinic instability process, because the deep anti-cyclonic eddy is found in the transition stage of the Kuroshio path from the straight to the oNLM path (not shown). This case, therefore, provides a good example of the transition from a straight to a meander path, although the amplitude of the meander is extremely large.

The cause of the successful prediction of the large meander is probably that seeds of the large meander, upper-layer eddies and the deep anticyclonic eddy, are introduced in the initial conditions. The upper-layer eddies, the warm eddy south of the Shikoku, and the cold eddy corresponding to the small meander south of the Kii Peninsula, are introduced by assimilating the observed data. The deep anticyclonic eddy, however, is not introduced directly by assimilation, because the system corrects the model field above 1,500 m by the assimilation as described in Section 2.2. Here we consider the formation process of the deep anticyclonic eddy seen in the initial conditions. Left panels in Fig. 11 show SSH and velocity at 3,000 m at the middle of May and the beginning of June 2004. Each panel shows a 5-day mean field of the assimilation result. At the middle of May 2004, a deep cyclonic eddy can be seen in the Shikoku Basin. In the upper layer, a warm eddy, coming from east of Amami-Oshima, and a cold eddy, are located east of the Tokara Strait and southeast of the Kyushu, respectively. After that, the deep anticyclonic
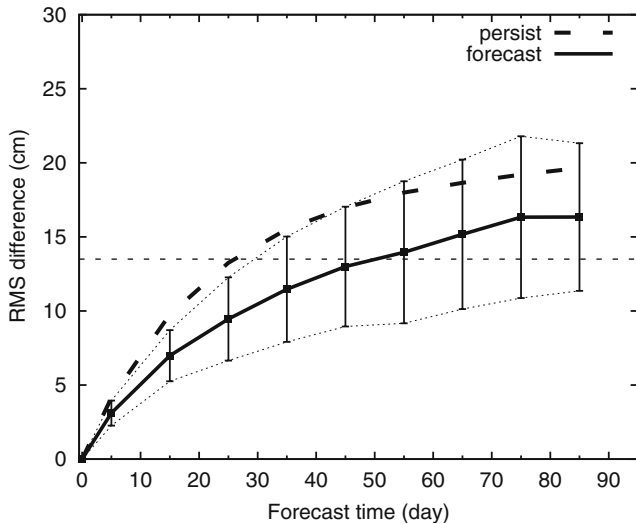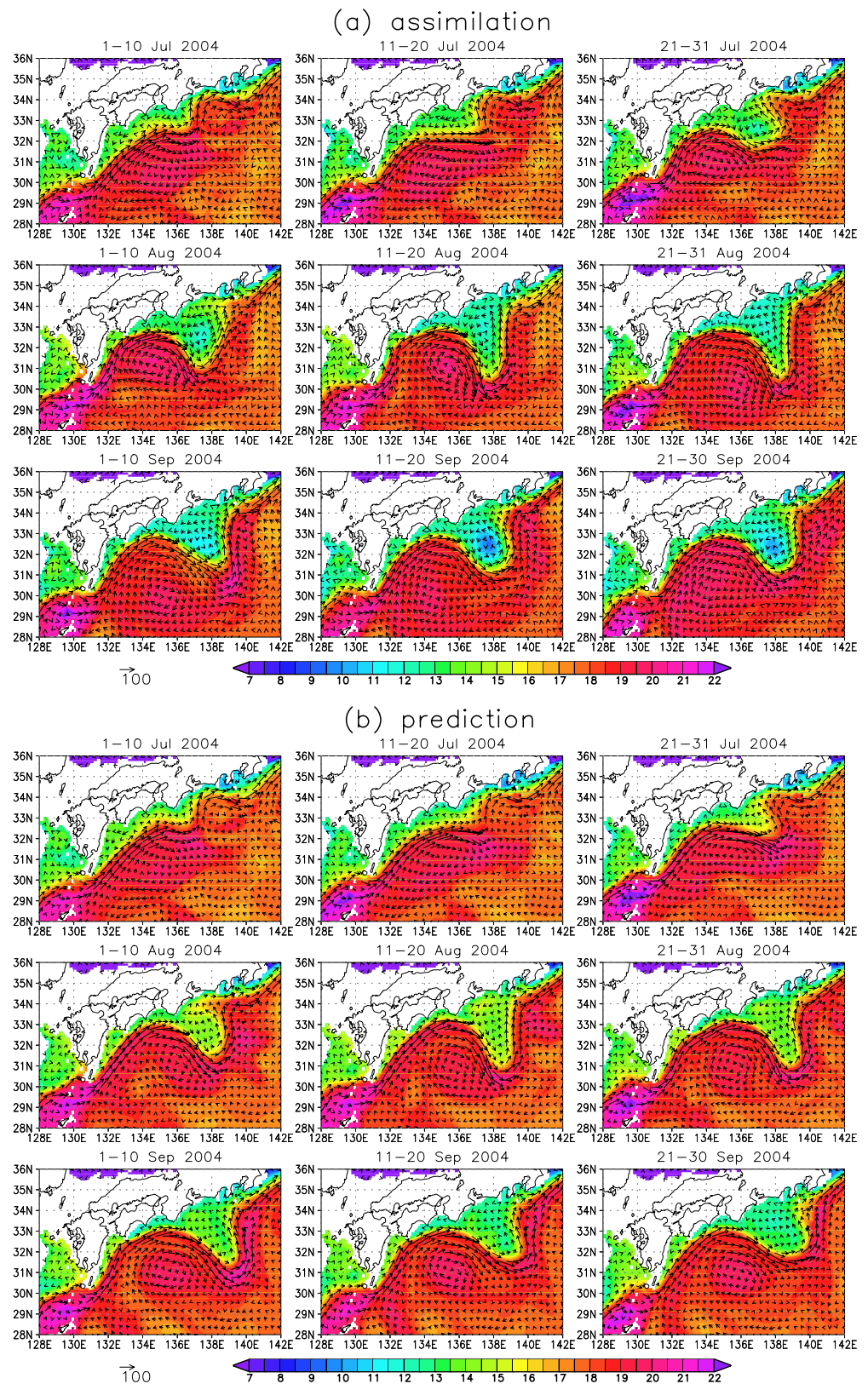
Fig. 9 Evolution processes of the large meander which occurred in August 2004 for **a** the assimilation and **b** the prediction fields initialized on 1 July 2004. Each panel shows mean fields of temperature (color; units in °C) and velocity (vector; units in cm s^{-1}) at 200 m over 1/3 month

eddy is formed between the upper-layer warm and cold eddies, and starts propagating eastward. In contrast, the deep cyclonic eddy disappears.

To understand the dynamics of this process, the vertical velocity at 2,000 m and the stretching term at 3,000 m in the vorticity equation are depicted in the middle and right
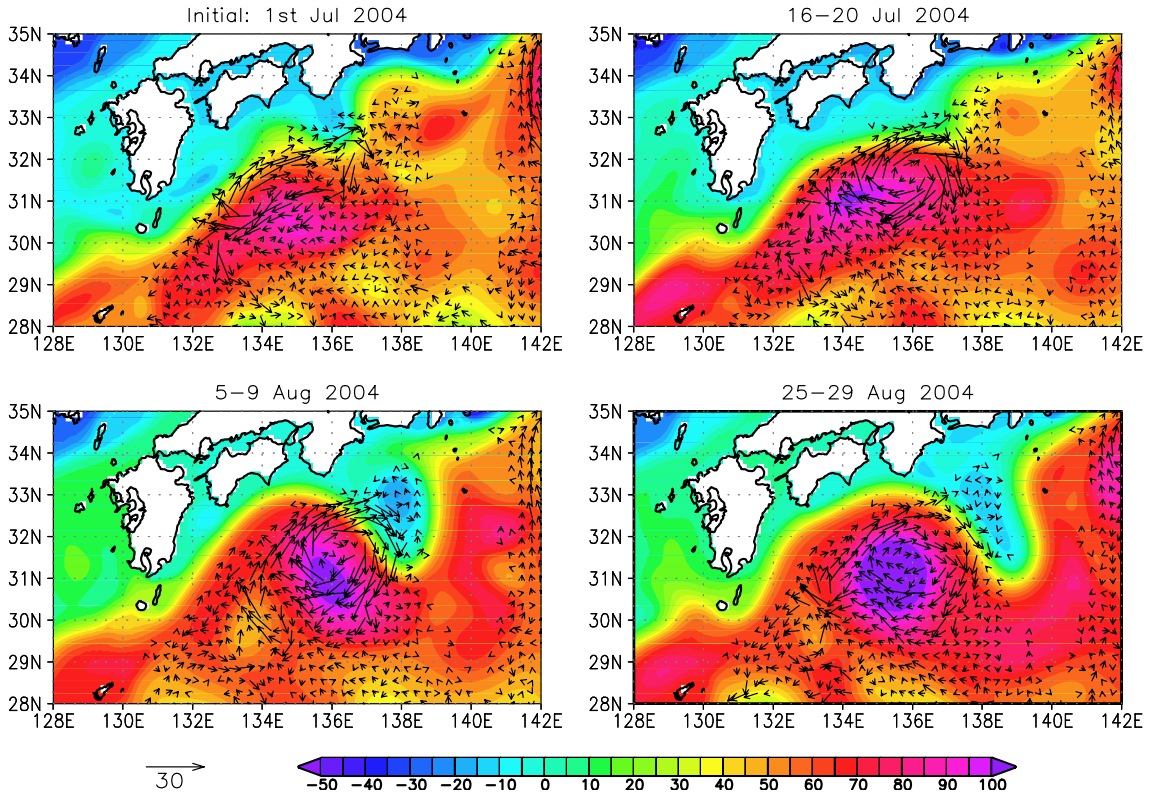
Fig. 10 The evolution process of the predicted large meander in August 2004. The prediction starts from 1 July 2004. Each panel shows SSH (color; units in cm) and velocity (vector; units in cm s^{-1}) at 3,000 m. The initial field shows a snapshot, and the predicted fields show the 5-day mean fields
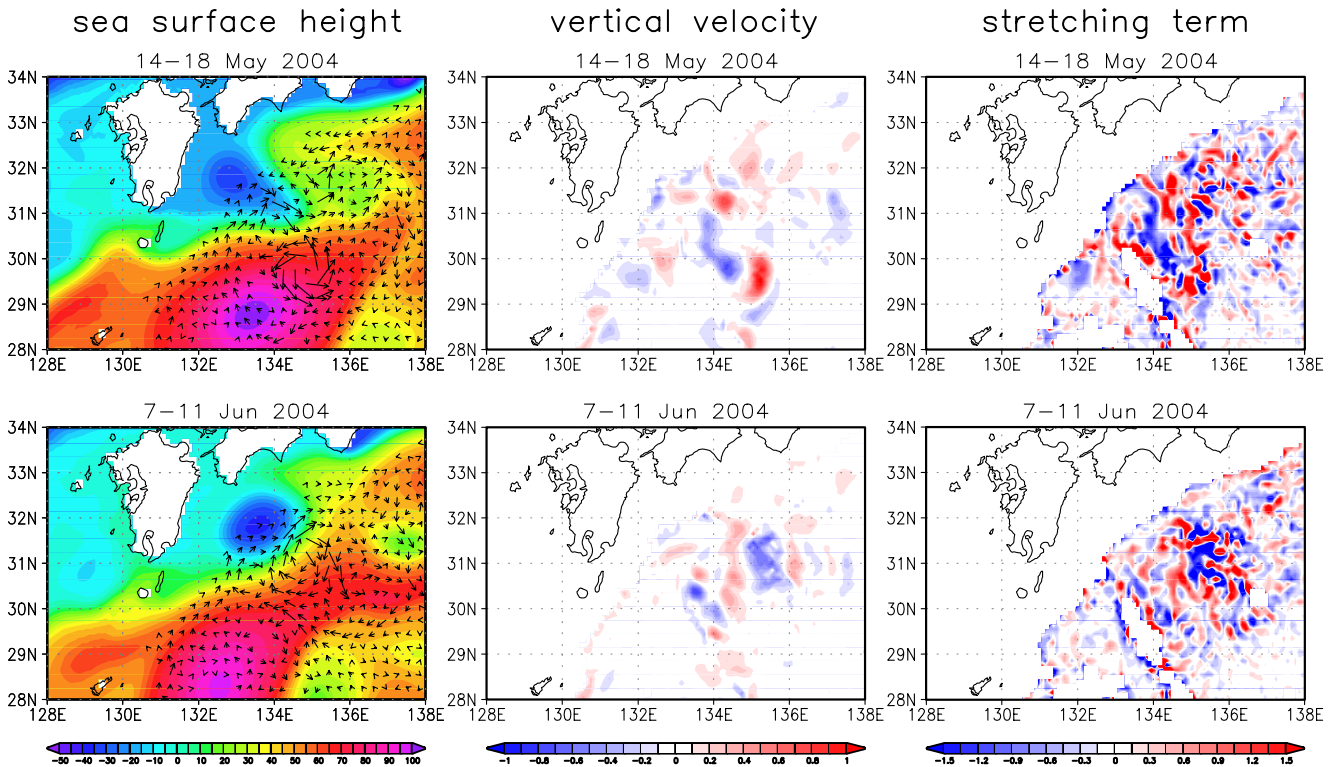
Fig. 11 The formation process of the deep anticyclonic eddy. *Left column*; 5-day mean fields of SSH (color; units in cm) and velocity (vector; units in cm s^{-1}) at 3,000 m. *Middle column*; vertical velocity (units in $\times 10^{-1}$ cm s^{-1}) field. *Right column*; the stretching term (units in $\times 10^{-11}$ s^{-1}) in the vorticity equation. Each panel shows 5-day mean fields over 14–18 May (*upper*) and 7–11 June 2004 (*lower*)
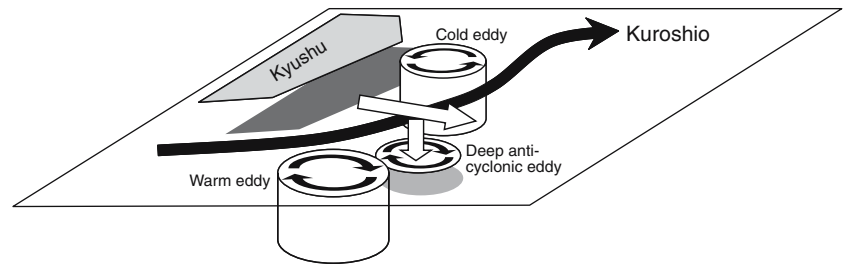
panels of Fig. 11. Each value is also estimated from the 5-day mean field of the assimilation result. At the middle of

May 2004, a downwelling at 2,000 m can be seen around $30°$ N and $134°$ E where the deep anticyclonic eddy is formed. The stretching term at 3,000 m in the vorticity equation, which plays a dominant role in the deep layer, shows a negative value there, indicating shrinking. At the beginning of June, the downward and upward flows with the shrinking and stretching in the deep layer can be seen on the east and the west sides of the deep anticyclonic eddy, respectively, causing the eastward propagation of the deep anticyclonic eddy. Therefore, the dynamics of the formation of the deep anticyclonic eddy can be explained by the following baroclinic process (see also Fig. 12): The warm eddy propagates northward toward the cold eddy located southeast of the Kyushu and an eastward flow between the warm and cold eddies is induced. Because the isotherms are tilted downward to the offshore across the Kuroshio, this eastward flow induces a downward flow in the deep layer. The induced downward flow generates the deep anticyclonic eddy by shrinking a vortex tube in the lower layer. This deep anticyclonic eddy then induces the downward and upward flows with the lower-layer shrinking and stretching to its east and west sides, respectively. As a result, the deep anticyclonic eddy propagates eastward and reaches south of the Kii Peninsula at the beginning of July 2004.

4.2 Case 2 (transition from a meander to a straight path)

Next, we present a prediction result initialized on 1 April 1993 as a typical example of failure. Figure 13 compares the Kuroshio axes between the assimilation and the prediction fields. The Kuroshio axis is defined by tracing the position of the maximum velocity at 100-m depth. In this case, the Kuroshio path is transformed from a meander into a straight path, but the transformation in the prediction occurs earlier than in the assimilation. In other words, the eastward propagation speed of the predicted meander is faster than that of the assimilation field. This is a common feature in many failure cases. In Section 3.2, we described the possibility that the downstream advection of the warm eddy south of the Kii Peninsula contributes to the transition of the Kuroshio axis from a meander to a straight path. But not all failure cases showing the same feature can be explained by this reasoning. We will further explore these failure cases by investigating the dynamical response of the model to the assimilation.

Figure 14a shows a SDH increment at the analysis time in the assimilation period of 21–31 May 1993. The

increment represents the difference between the SDHs estimated from the first-guess and analysis using Eq. (3). SSH tendencies at the forecast time FT=3, 8, and 13 days are also shown in Fig. 14b–d. SSH differences per day are regarded as SSH tendencies here. A large positive SDH increment can be seen on the western side of the Izu Ridge, and a negative SDH increment can be seen to the west of the positive increment. These positive and negative increments are located in the northward and southward flow on the eastern and western sides of the meander, respectively. The SSH tendency has an opposing signal at the same place as the SDH increment, which is quite large in the early stage of the prediction. It probably implies an initial shock caused by dynamically unbalanced initial conditions. In addition, the initial shock can lead to a faster eastward propagation of the meander, because the negative signal of the SSH tendency in the east side of the meander induces a cyclonic anomaly in the flow field and vice versa (see Fig. 15).

To confirm this, we conducted a parameter sensitivity experiment. If the parameter μ in Eq. (2) is set to a large (small) value, the assimilation result is largely affected by the first-guess (observation) field. The initial shock, therefore, is expected to be reduced by setting μ to a large value. In this sensitivity experiment, the parameter μ

is set to 0.9, which is much larger than 0.4, the default value in the prediction experiment. Using this value, the assimilation procedure is performed again from 1 January to 31 March 1993, and the initial condition on 1 April 1993 is regenerated. Using the regenerated initial condition, the 90-day prediction is also reconducted. Figure 16 shows the SSH tendency at the 3-day forecast time and the Kuroshio axes of the assimilation and the prediction on 1–10 May 1993. In the case of $\mu = 0.9$, the initial shock weakens compared to Figs. 14b and 16b. As a result, the eastward propagation speed of the meander is improved, and is almost the same as that of the assimilation field (Fig. 16a). We also tested the parameter $\mu = 0.9$ on another case, initialized on 1 November 1999, with the same features as in case 2. The eastward propagation speed of the meander is also improved. For these cases, the reduction of the initial shock is crucial for the improvement of the prediction of the Kuroshio path. It should be noted, however, that $\mu = 0.9$ is not necessarily the most suitable for the prediction because the reproducibility of a real ocean in the initial condition degenerates instead of reducing the initial shock. We, therefore, need further tuning on the parameter μ. In the future, we aim to reduce the initial shock more effectively by adding a dynamical
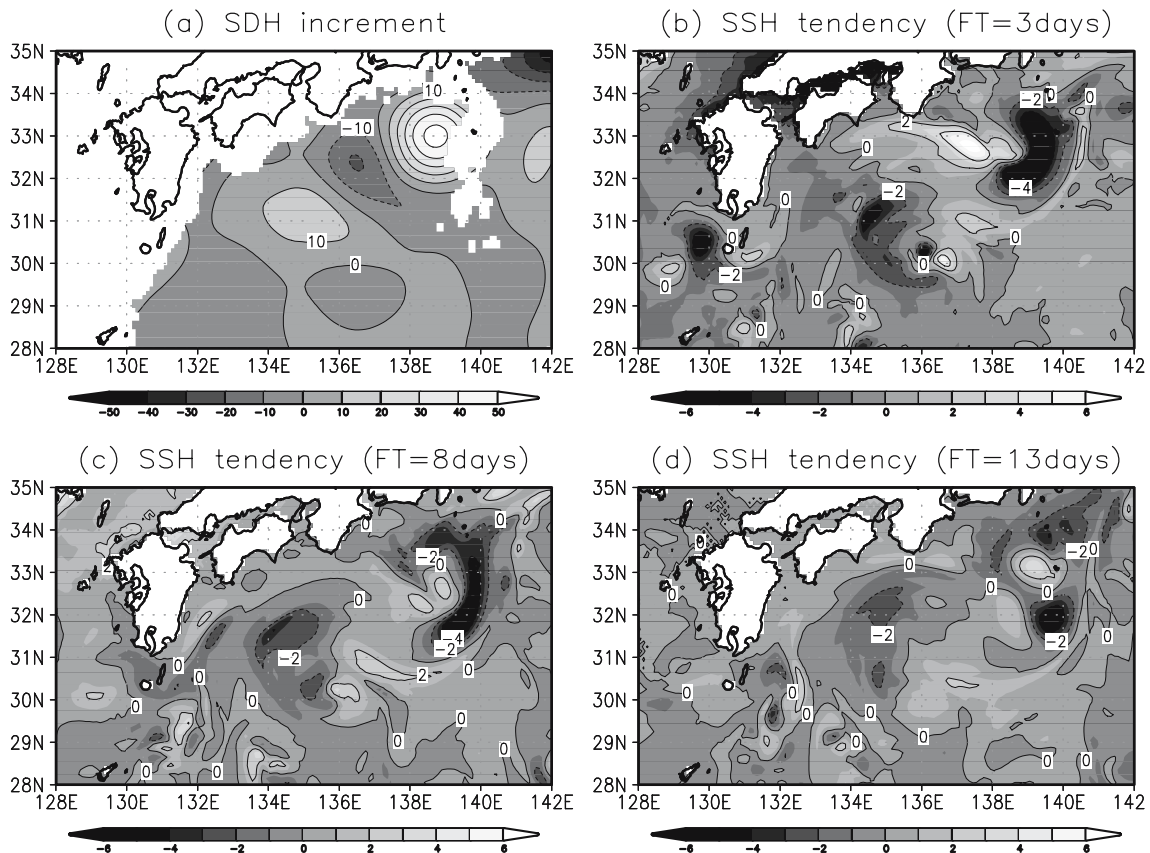

Fig. 14 The SDH increment (unit in cm) at the analysis time in the assimilation period of 21–31 May 1993 and the time evolution of SSH tendencies (units in cm day^{-1}). **a** The SDH increment denotes the difference between SDHs estimated from the first-guess and analysis fields. SSH tendencies at the forecast time FT=3–13 days are depicted in **b**–**d**. SSH differences per day are regarded as SSH tendencies
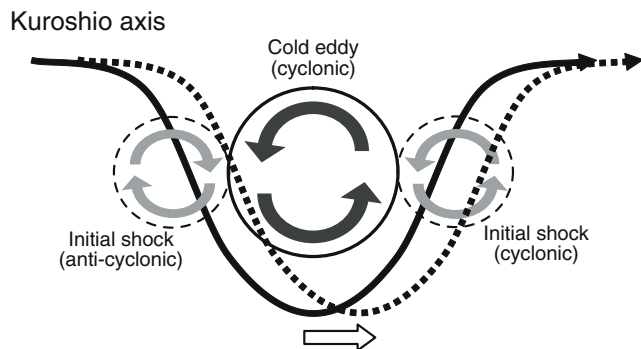
Kuroshio axis

Fig. 15 Schematic diagram of the relation between the initial shock and the eastward propagation of the meander

constraint to the cost function or by improving the method of inserting analysis increments into the model.

4.3 Case 3 (unrealistic meander)

Lastly, we present a prediction result initialized on 1 September 1996 as an example of a failure with an
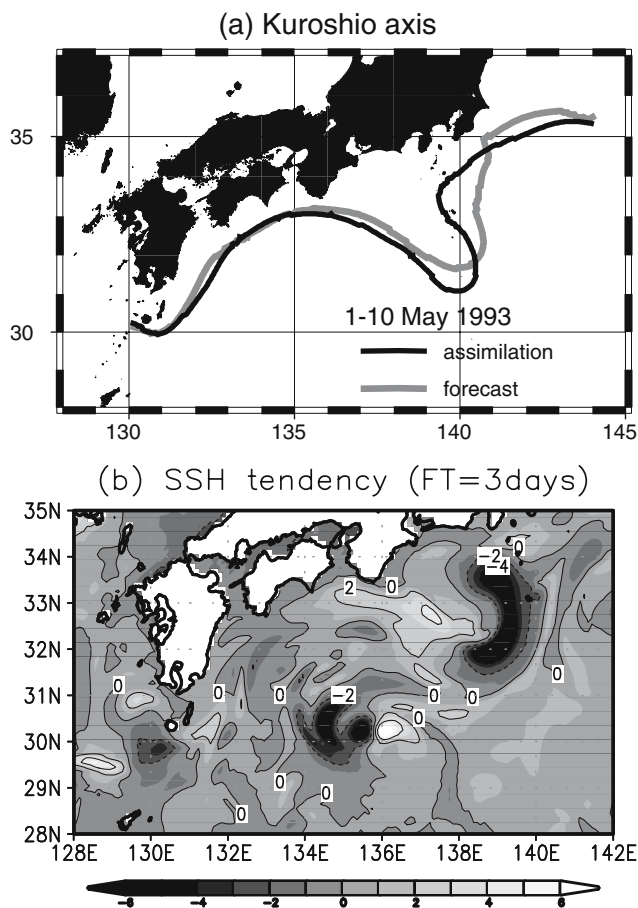

Fig. 16 The Kuroshio axes and SSH tendency in the case of $\mu = 0.9$. **a** Comparison of the Kuroshio axes at the begging of May 1993 between the assimilation (*black line*) and the prediction (*gray line*) fields initialized on 1 April 1993. **b** The SSH tendency (units in cm) at the forecast time FT=3 days

unrealistic meander. Figure 17 compares the SSH fields from September to November 1996 between the assimilation and the prediction fields. The Kuroshio in the assimilation field shows a straight path during the whole period. On the contrary, the predicted Kuroshio has a small meander at the beginning of October that develops into a large meander. To explore what causes this unrealistic meander, we look at the error evolution. Figure 18 shows the time evolution of the normalized difference of temperature at 1,000 m between the prediction and assimilation fields. The standard deviation of temperature, calculated from the assimilation results from 1993 to 2004, is used to normalize the temperature difference. In the early stage of the prediction, a cold anomaly southeast of the Kyushu, which appears to be introduced by assimilating in situ data in the middle of August, can be seen only in the intermediate layer. This anomaly then extends in the vertical direction and leads to an upper-layer cold eddy southeast of Kyushu. The cold eddy then interacts with a warm eddy, which comes from east of the Tokara Strait and induces a deep anticyclonic eddy between these two eddies (not shown). The cold eddy then grows rapidly and appears to propagate along the Kuroshio (Fig. 18). This evolution process is very similar to the time evolution of the normalized SSH RMS difference described in Section 3.2 with Fig. 6. Consequently, the cold eddy develops into a large meander, which is probably caused by the baroclinic instability, as in case 1.

It is possible that the intermediate cold anomaly seen in the early stage of the prediction may correspond to an unstable mode, which gives rise to the unrealistic meander. In fact, the meander does not occur in the prediction experiment initialized on 1 August 1996 before the intermediate cold anomaly is assimilated. It should be emphasized that this unrealistic meander occurs though an error in the initial conditions is not so large. This fact probably implies that the Kuroshio path south of Japan has a chaotic nature, which makes the prediction of the Kuroshio difficult. However, we can recognize in advance such an unstable mode in an initial condition by applying some initializing methods for an ensemble prediction, such as breeding (e.g., Toth and Kalnay 1997) or singular vector (e.g., Molteni et al. 1996; Moore and Mariano 1999) methods. We may be able to improve the predictive limit of the Kuroshio path south of Japan using such initializing methods.

5 Summary

We conducted assimilation and prediction experiments of the Kuroshio path variability south of Japan using an eddy-resolving model and a 3DVAR with vertical coupled T–S EOF modes. The SSH variability and the variations of the Kuroshio path of the assimilation fields are in a good agreement with the observations. The statistical properties of the prediction results of 138 cases are investigated. The prediction results have relatively large errors southeast of Kyushu and off Enshu-nada, which are mostly caused by

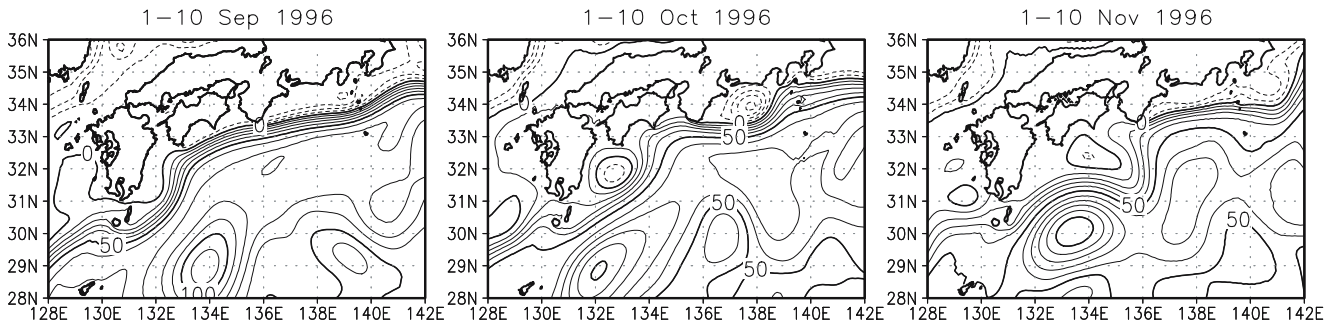## (a) assimilation
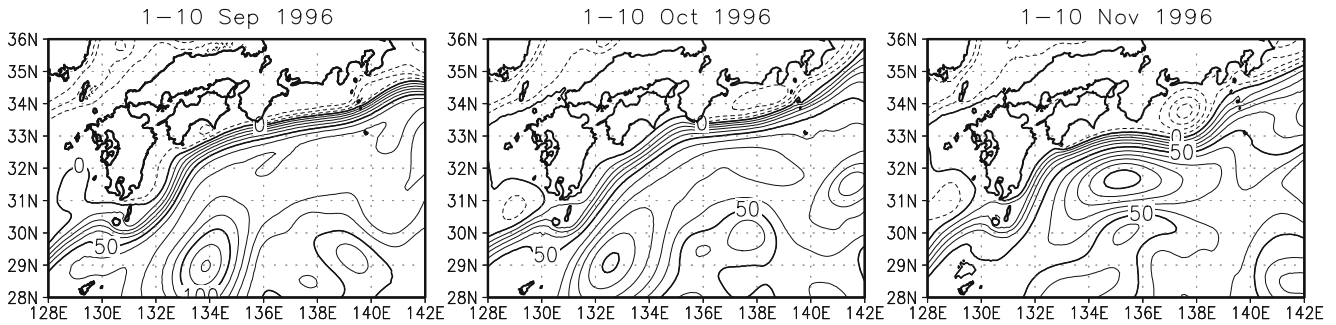
(b) prediction

Fig. 17 Time evolution of the 10-day mean SSH (units in cm) fields of **a** the assimilation and **b** the prediction fields initialized on 1 September 1996

random errors. The predictive limit of our system assessed by SSHA in the assimilation field is roughly 40–60 days, which is much longer than that of the persistence.

The performance of the prediction depends on the transition stages of a meander, as reported in previous studies. That is, it shows a relatively good performance in the transition stage from a straight to a meander path, while the performance of the prediction deteriorates in the transition stage from a meander to a straight path. Also, some predictions show unrealistic meanders. These features are investigated with case studies.

The large meandering event that occurred in August 2004 is successfully predicted in a 2-month forecast. The large meander is caused by the interaction between upper- and lower-layer eddies, that is, by baroclinic instability. This formation process of the meander is consistent with that of Tsujino et al. (2006). The reason for such a successful prediction of the large meander is probably that seeds of the large meander, upper-layer eddies and the deep anticyclonic eddy, are introduced in the initial condition. The formation process of the deep anticyclonic eddy, which is not introduced directly by assimilation, is also investigated. It is formed through the baroclinic process as a result of interaction between the upper-layer warm and cold eddies, which are introduced by the assimilation.

Next, we investigate the case of the transition stage from a meander to a straight path. In this case, the eastward propagation speed of the meander is faster than a real state.

This is a common feature seen in many failure cases. By considering the dynamical response of the model to the assimilation, it is revealed that the initial shock caused by the dynamically unbalanced initial condition induces the eastward propagation of the meander. In fact, reducing the initial shock by tuning an assimilation parameter yields improvements to the eastward propagation speed of the meander.

Finally, we investigate the case of an unrealistic meander. In this case, a cold anomaly around 700–1,000 m in the initial condition, which is introduced by the assimilation, grows rapidly and results in an unrealistic meander. The important thing in this case is that the unrealistic meander occurs though the error in the initial condition is not so large. This probably implies that the Kuroshio path south of Japan has a chaotic nature, which makes the prediction of the Kuroshio difficult.

The details of these failure cases give us some insight for improving the predictive skill of the Kuroshio path variability. To reduce the initial shock, we need to optimize the assimilation parameters. In addition, we may be able to reduce the initial shock effectively by adding a dynamical constraint to the cost function or by improving the method of inserting analysis increments into the model. To prevent a wrong forecast with an unrealistic meander, an ensemble prediction using initializing methods such as breeding and singular vector may be effective. These improvements should be subjects of future studies.
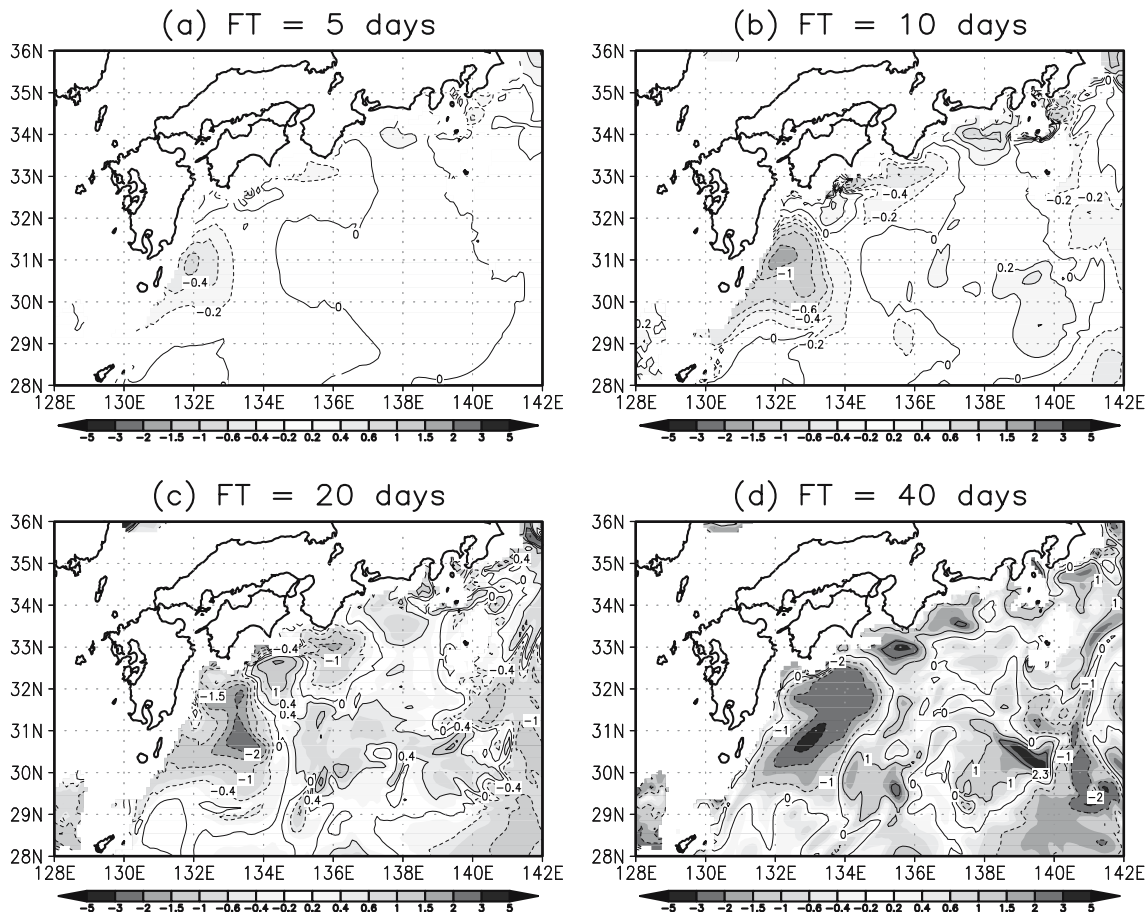
622

Fig. 18 Time evolution of the normalized difference of temperature field at 1,000 m between the prediction initialized on 1 September 1996 and the assimilation fields. The units are nondimensional

References

Akitomo K, Masuda S, Awaji T (1997) Kuroshio path variation south of Japan: stability of the paths in a multiple equilibrium regime. J Oceanogr 53:129–142

Ambe D, Imawaki S, Uchida H, Ichikawa K (2004) Estimating the Kuroshio axis south of Japan using combination of satellite altimetry and drifting buoys. J Oceanogr 60:375–382

Arakawa A (1966) Computational design for long-term numerical integration of the equations of fluid motion: two-dimensional incompressible flow. Part I. J Comput Phys 1:119–143

Bloom SC, Takacs LL, Da Silva AM, Ledvina D (1996) Data assimilation using incremental analysis updates. Mon Weather Rev 124:1256–1271

Brasseur P, Blayo E, Verron J (1996) Predictability experiments in the North Atlantic Ocean: outcome of a quasi-geostrophic model with assimilation of TOPEX/POSEIDON altimeter data. J Geophys Res 101:14161–14174

Collecte, Localisation, Satellites (CLS) (2004) SSALTO/DUACS user handbook: (M)SLA and (M)ADT near-real time and delayed time products. CLS-DOS-NT-04.103, Toulouse, p 42

Ebuchi N, Hanawa K (2001) Trajectory of mesoscale eddies in the Kuroshio recirculation region. J Oceanogr 57:471–480

Ebuchi N, Hanawa K (2003) Influence of mesoscale eddies on variations of the Kuroshio path south of Japan. J Oceanogr 59:25–36

Endoh T, Hibiya T (2000) Numerical study of the generation and propagation of trigger meanders of the Kuroshio south of Japan. J Oceanogr 56:409–418

Endoh T, Hibiya T (2001) Numerical simulation of the transient response of the Kuroshio leading to the large meander formation south of Japan. J Geophys Res 106:26833–26850

Fujii Y (2005) Preconditioned optimizing utility for large-dimensional analyses (POpULar). J Oceanogr 61:167–181

Fujii Y, Kamachi M (2003a) Three-dimensional analysis of temperature and salinity in the equatorial Pacific using a variational method with vertical coupled temperature–salinity EOF modes. J Geophys Res 108(C9):3297 DOI:10.1029/2002JC001745

Fujii Y, Kamachi M (2003b) A reconstruction of observed profiles in the sea east of Japan using vertical coupled temperature–salinity EOF modes. J Oceanogr 59:173–186

Fujii Y, Kamachi M (2003c) A nonlinear preconditioned quasi-Newton method without inversion of a first-guess covariance matrix in variational analysis. Tellus 55A:450–454

Fujii Y, Ishizaki S, Kamachi M (2005) Application of nonlinear constraints in a three-dimensional variational ocean analysis. J Oceanogr 61:655–662

Fukumori I (2002) A partitioned Kalman filter and smoother. Mon Weather Rev 130:1370–1383

Griffies SM, Hallberg RW (2000) Biharmonic friction with a Smagrinsky-like viscosity for use in large-scale eddy-permitting ocean models. Mon Weather Rev 128:2935–2946

Hamilton D (1994) GTSPP builds an ocean temperature–salinity database. Earth Syst Monit 4(4):4–5

Holland WR, Chow JC, Bryan FO (1998) Application of a third-order upwind scheme in the NCAR ocean model. J Climate 11:1487–1493

Hunke EC, Ducowicz JK (2002) The elastic–viscous–plastic model for sea ice dynamics. Mon Weather Rev 130:1848–1865

Hurlburt HE, Wallcraft AJ, Schmitz WJ, Hogan PJ, Metzger EJ (1996) Dynamics of the Kuroshio/Oyashio current system using eddy-resolving models of the North Pacific Ocean. J Geophys Res 101:941–976

Hurlburt HE, Smedstat OM, Rhodes RC, Cayula J-F, Barron CN, Metger EJ (2000) A feasibility demonstration of ocean model eddy-resolving nowcast/forecast skill using satellite altimeter data. NRL MR 7320-00-8235, Naval Research Laboratory, Stennis Space Center, Hancock, p 23

Imawaki S, Gotoh M, Yoritaka H, Yoshioka N, Misumi A (1996) Detecting fluctuations of the Kuroshio axis south of Japan using TOPEX/POSEIDON altimeter data. J Oceanogr 52:69–92

Ishikawa I, Tsujino H, Hirabara M, Nakano H, Yasuda T, Ishizaki H (2005) Meteorological Research Institute Community Ocean Model (MRI.COM) manual. Technical reports of the Meteorological Research Institute, No.47. Meteorological Research Institute, Ibaraki (in Japanese)

Ishizaki H, Motoi T (1999) Reevaluation of the Takano–Oonishi schemes for momentum advection on bottom relief in ocean models. J Atmos Ocean Technol 16:1994–2010

Kamachi M, Kuragano T, Sugimoto S, Yoshita K, Sakurai T, Nakano T, Usui N, Uboldi F (2004) Short-range prediction experiments with operational data assimilation system for the Kuroshio south of Japan. J Oceanogr 60:269–282

Kanamitsu M, Ebisuzaki W, Woollen J, Yang S-K, Hnilo JJ, Fiorino M, Potter GL (2002) NCEP-DOE AMIP-II reanalysis(R-2). Bull Am Meteorol Soc 83:1631–1643

Kawabe M (1985) Sea level variations at the Izu Islands and typical stable paths of the Kuroshio. J Oceanogr Soc Japan 41:307–326

Kawabe M (1987) Spectral properties of sea level and time scale of Kuroshio path variations. J Oceanogr Soc Japan 43:111–123

Kawabe M (1995) Variations of current path, velocity, and volume transport of the Kuroshio in relation with the large meander. J Phys Oceanogr 25:3103–3117

Killworth PD, Stainforth D, Webb DJ, Paterson SM (1991) The development of a free-surface Bryan–Cox–Semtner ocean model. J Phys Oceanogr 21:1333–1348

Komori N, Awaji T, Ishikawa Y, Kuragano T (2003) Short-range forecast experiments of the Kuroshio path variabilities south of Japan using TOPEX/Poseidon altimetric data. J Geophys Res 108(C1):3010 DOI:10.1029/2001JC001282

Kondo J (1975) Air-sea bulk transfer coefficients in diabatic conditions. Boundary-Layer Meteorol 9:91–112

Kuragano T, Kamachi M (2000) Global statistical space-time scales of oceanic variability estimated from the TOPEX/POSEIDON altimetry data. J Geophys Res 105:955–974

Kuragano T, Kamachi M (2003) Altimeter's capability of reconstructing realistic eddy fields using space-time optimum interpolatio. J Oceanogr 59:765–781

Masuda A (1982) An interpretation of the bimodal character of the stable Kuroshio path. Deep-Sea Res 29:471–484

Mellor GL, Ezer T (1991) A Gulf Stream model and an altimetry assimilation scheme. J Geophys Res 96:8779–8795

Mellor GL, Kantha L (1989) An ice-ocean coupled model. J Geophys Res 94:10937–10954

Mitsudera H, Waseda T, Yoshikawa Y, Taguchi B (2001) Anti-cyclonic eddies and Kuroshio meander formation. Geophys Res Lett 28:2025–2028

Miyazawa Y, Guo X, Yamagata T (2004) Roles of mesoscale eddies in the Kuroshio paths. J Phys Oceanogr 34:2203–2222

Molteni F, Palmer TN, Petroliagis T (1996) The ECMWF ensemble prediction system: methodology and validation. Q J R Meteorol Soc 122:73–119

Moore AM, Mariano AJ (1999) The dynamics of error growth and predictability in a model of the gulf stream. Part I: singular vector analysis. J Phys Oceanogr 29:158–176

Noh Y, Kim H-J (1999) Simulations of temperature and turbulence structure of the oceanic boundary layer with the improved near-surface processes. J Geophys Res 104:15621–15634

Ocean Climate Laboratory (1999) World Ocean Atlas 1998 (WOA98) CD-ROM documentation version 1.0. Ocean Climate Laboratory, National Oceanographic Data Center, Silver Spring

Qiu B, Miao W (2000) Kuroshio path variation south of Japan: bimodality as a self-sustained internal oscillation. J Phys Oceanogr 30:2124–2137

Rhodes RC, Hurlburt HE, Wallcraft AJ, Barron CN, Martin PJ, Metzger EJ, Shriver JF, Ko DS, Smedstad OM, Cross SL, Kara AB (2002) Navy real-time global modering systems. Oceanography 15(1):29–43 (special issue—Navy operational models: ten years later)

Robinson AR, Taft BA (1972) A numerical experiment for the path of the Kuroshio. J Mar Res 30:65–101

Sekine A (1990) A numerical experiment on the path dynamics of the Kuroshio with reference to the formation of the large meander path south of Japan. Deep-Sea Res 37:359–380

Smith WHF, Sandwell DT (1997) Global sea floor topography from satellite altimetry and ship depth soundings. Science 277:1956–1962

Spall MA, Holland WR (1991) A nested primitive equation model for oceanic applications. J Phys Oceanogr 21:205–220

Taft BA (1972) Characteristics of the flow of the Kuroshio south of Japan. In: Stommel H, Yoshida K (eds) Kuroshio—its physical aspects. University of Tokyo Press, Tokyo, pp 165–216

Toth Z, Kalnay E (1997) Ensemble forecasting at NCEP and the breeding method. Mon Weather Rev 125:3297–3319

Tsujino H, Usui N, Nakano H (2006) Dynamics of Kuroshio path variations in a high-resolution GCM. J Geophys Res (in revision)

Usui N, Ishizaki S, Fujii Y, Tsujino H, Yasuda T, Kamachi M (2006) Meteorological Research Institute multivariate ocean variational estimation (MOVE) system: some early results. Adv Space Res 37:806–822

Waseda T, Mitsudera H, Taguchi B, Yoshikawa Y (2003) On the eddy–Kuroshio interaction: meander formation process. J Geophys Res 108(C7):3220 DOI:10.1029/2002JC001583

Weatherly GL (1972) A study of the bottom boundary layer of the Florida current. J Phys Oceanogr 2:54–72

Yoon J-H, Yasuda I (1987) Dynamics of the Kuroshio large meander: two-layer model. J Phys Oceanogr 17:66–81

Yoshida S (1964) A note on the variations of the Kuroshio during recent years. Bull Jpn Soc Fish Oceanogr 5:66–69 (in Japanese)